Inertial and Interfacial Effects on Pressure Drop of Taylor Flow in Capillaries

Michiel T. Kreutzer, Freek Kapteijn, and Jacob A. Moulijn
Reaction and Catalysis Engineering, DelftChemTech, Faculty of Applied Sciences, Delft University of Technology, Julianalaan 136, 2628 BL Delft, The Netherlands

Chris R. Kleijn
Dept. of Multiscale Physics, Faculty of Applied Sciences, Delft University of Technology, Prins Berhardlaan 6, 2628 BW Delft, The Netherlands

Johan J. Heiszwolf
Air Products and Chemicals, Inc., 7201 Hamilton Blvd., Allentown PA, 18195

DOI 10.1002/aic.10495
Published online July 7, 2005 in Wiley InterScience (www.interscience.wiley.com).

In a capillary, the two-phase pressure drop in Taylor slug flow was measured. A carefully designed inlet section for the capillary allowed the independent variation of gas bubble and liquid slug length. Gas and liquid superficial velocities were varied from 0.04 m/s to 0.3 m/s. If the slug length was smaller than 10 times the capillary diameter, the length-averaged friction factor for the liquid slug increased drastically from the single phase value ($f = 16/Re$) due to differences in curvature at the front and the back of the bubble. The use of different liquids allowed the independent variation of Re and Ca. The flow of elongated bubbles in capillaries was simulated using the CFD code FIDAP. It was found both numerically and experimentally that for $Re \gg 1$, the extra pressure terms may be taken account using (Ca/Re) as a parameter. The numerical results agreed with the experimental data, provided that Marangoni effects of impurities are taken into account. The results allow the determination of slug length from pressure drop measurements in closed equipment where the slug length cannot otherwise be measured easily, such as monoliths and microreactors. © 2005 American Institute of Chemical Engineers *AIChE J,* 51: 2428–2440, 2005

Keywords: pressure drop, microchannels, Taylor flow, Bretherton's problem, monoliths, capillary, multiphase flow.

Introduction

Monoliths catalyst structures are increasingly considered for multiphase reactor applications.[1–3] The applications include Fischer-Tropsch synthesis,[4,5] and the hydrogenation of α-methylstyrene,[6–8] phenylacetylene,[9] fats and oils,[10] sorbitol[11] and nitroaromatics.[12]

Monoliths are structured catalyst supports, that is, they have a regular well-defined geometry. The structure may be regarded as an array of parallel straight small channels, having a diameter of the order of 1 mm, generally separated by thin walls, having a thickness of about one tenth of the channel diameter. The advantages of monoliths for multiphase applications are similar to the advantages in the classical gas-only uses of monoliths: (1) the open structure without bends hardly

Correspondence concerning this article should be addressed to M. T. Kreutzer at kreutzer@tnw.tudelft.nl.

© 2005 American Institute of Chemical Engineers

obstructs the flow, and a low pressure drop can be achieved in a structure of high surface area, and (2) thin catalyst coatings reduce diffusional limitations.

In multiphase monoliths, the predominant flow pattern is a bubble-train flow of elongated bubbles. The theory of these elongated bubbles is a classical problem in fluid mechanics, referred to as *Bretherton's problem*[13] or *Taylor Flow*.[14] The pressure drop in Taylor flow is indeed very low compared to randomly packed beds of similar geometric surface area.[15] Furthermore, it has been shown that the hydrodynamics of Taylor flow allow for good mass-transfer rates from the bubbles to the liquid,[16,17] and spectacular mass transfer from the bubbles to the wall.[18] Increasingly, the benefits of Taylor flow are recognized outside the field of monoliths, especially in the microfluidics and microreactor community.[19,20]

The aim of this work was the development of an accurate pressure drop model for Taylor flow in monolith reactors. There are several reasons why such a model is highly desired. The most obvious one, the prediction of the pressure drop over a reactor column so compressors and pumps for that reactor may be designed, is the least important. The pressure drop over the column is low (or even zero), so the design of pump and compressors is not critical, and one might be contented with the less accurate models that are available. This work was motivated by other considerations, which are

- Taylor flow can exhibit highly undesired dynamic oscillations that may grow to significant instability. The behavior can be predicted if the gradients of pressure drop versus gas and liquid flow rate are accurately known,[21] and stability criteria for monoliths can be then formulated.[22,23]
- Monoliths can be operated in a loop reactor configuration,[2,15] where a compressor can be eliminated and the gas circulation is induced by the suction of the downward bubble train flow. Now the pressure drop is approximately zero, and a pressure drop model is required to predict the gas circulation flow rate.
- Horvath et al.[24] demonstrated that the pressure drop in Taylor flow depends on the slug length. The slug length is an important parameter in predicting the mass transfer rate,[7,16,17,24] and physical intuition predicts that more bubbles per unit channel length (that is, shorter slugs) will result in a higher pressure drop. Then, because this effect is apparently significant, pressure drop measurements can be used to obtain the slug length.
- A model for the residence time distribution in monoliths may be constructed from the notion that in all the channels, the pressure drop must be the same.[23]

For all these considerations, we need an accurate model for the pressure drop. For an order-of-magnitude estimate of the pressure drop in two-phase flow in randomly packed reactors, the approach of Lockhart and Martinelli,[25] or a homogeneous model approach is most frequently used. Surface tension effects, which are quite naturally absent in single phase pressure drop, are always missed by approaches like Lockhart-Martinelli that estimate two-phase pressure drop from single phase results. Chen et al.[26] collected 11 sets of literature data for two-phase pressure drop in small diameter tubes, and found that even if surface tension was included in the model by a Weber number or a Capillary number, neither Lockhart–Martinelli models nor homogeneous pressure drop models accurately predicted the data.

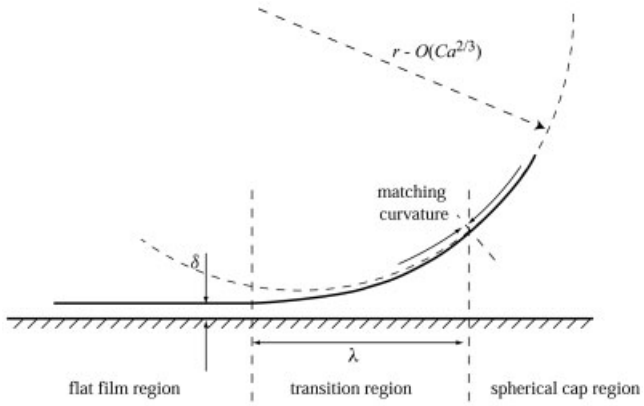

Figure 1. Representation of the transition region between the flat film and the spherical front of the bubble.[13]

Both the homogeneous model and the Lockhart–Martinelli model use little information about the two-phase flow pattern. The advantage is that no specific knowledge of the flow pattern is required to predict the pressure drop, and the—related and obvious—disadvantage is that no information about the flow pattern can be obtained from experimental pressure drop data. In Taylor flow, the information that is specific to the flow pattern is the amount of bubbles per unit length of channel, that is, the bubble frequency. The average bubble and slug length may be obtained from the bubble frequency in a straightforward manner. In Taylor flow, the slugs are sealed between the bubbles, preventing coalescence, and the length of a slug formed at the entrance of the channel remains constant over the entire length of the channel. The same holds for the bubble length, and the two-phase Taylor flow pattern in a capillary is fully characterized and determined by the bubble frequency, the liquid superficial velocity, the gas superficial velocity and the fluid properties. The aim of this work can thus be reformulated as: the development of a pressure drop model for Taylor flow in capillaries that takes the slug and bubble length into account and allows the slug length to be determined from experimental pressure drop data.

Previous Work on an Elongated Bubble in a Capillary

Bretherton[13] pioneered the use of a lubrication analysis for the transitional region where the film is formed, that is, between the spherical front of the bubble and the flat film far behind the front (Figure 1). The front of the bubble may be regarded as spherical with a radius equal to the tube radius r, so the Laplace pressure difference across the gas–liquid interface is given by $\Delta p = 2\gamma/r$, provided the film thickness is small ($\delta \ll r$). In the region of constant film thickness, the curvature in the axial direction vanishes, and the Laplace pressure difference is given by $\Delta p = \gamma/r$. A balance of the viscous force and the pressure gradient in the transitional region eventually yields (For a more extensive analysis, see for example, the original Bretherton[13] or the more recent review by Chang[27])

$$\frac{\delta}{d} = 0.66Ca^{2/3} \tag{1}$$

The method developed by Bretherton also gave an expression for the pressure drop over the bubble: the real curvature of the nose is smaller than $2/r$ by an amount $\mathbb{O}(Ca^{2/3})$. A similar analysis may be made for the rear of the bubble, and the pressure drop over the bubble is then $\mathbb{O}((2\gamma/r)Ca^{2/3})$. Bretherton found

$$\Delta p = 7.16(3Ca)^{2/3}\left(\frac{\gamma}{d}\right) \tag{2}$$

Bretherton measured the film thickness by monitoring the decrease in volume of a single liquid slug that propagated through an empty tube. Remarkably, the $Ca^{2/3}$ scaling law was confirmed for higher Capillary numbers using benzene and aniline as liquids, but for Ca lower than 10^{-3}, the film thickness was substantially larger than the theory predicted.

Ratulowski and Chang[28] showed that the Marangoni effect of trace impurities explains the discrepancy between the experimental data and Bretherton's theory. In regions of low surfactant concentration, the interface is mobile and a no-shear boundary condition is valid at the gas–liquid interface. At regions of high surfactant concentration, the interface becomes rigid—Bretherton used the term "hardening of the surface"—and a no-slip boundary condition is more appropriate to describe the gas liquid interface in the transition region. Bretherton had already shown that by using a no-slip boundary condition at the interface for a new lubrication analysis, both the pressure drop over the bubble and the film thickness increase by a factor $4^{2/3}$. The true behavior of the interface is in fact very complex[29,30] but all experimental data is bounded by the no-shear and no-slip limits.

The theory of Bretherton has been confirmed by numerous numerical studies, in which, of course, ideal circumstances without impurities can easily be modeled,[31–37] which all confirm Bretherton's analysis for low Ca, and all have similar results for the film thickness and pressure drop at higher Ca. Most of these studies have ignored inertial effects, which is reasonable if $We \ll 1$, where $We = ReCa$ is the Weber number. In recent work on Bretherton's problem, the effect of inertia, which readily becomes important for low-viscosity liquids, has been analyzed numerically in greater detail for Re up to about 200.[34–37] In most of the experimental studies reported in the literature, the Capillary number is varied by increasing the liquid viscosity, so the Reynolds number is always low. The only experimental data at high Reynolds numbers were recently reported by Aussilous and Quére,[38] who measured a noticeable increase in film thickness with respect to the Bretherton value at high velocity and low viscosity.

All studies agree that inertia has a considerable impact on the bubble shape. The pressure drop over a single bubble is largely determined by the Laplace pressure term, which in turn is governed by the bubble shape, and we expect a strong influence of inertia on the pressure drop.

It is interesting to note that in the engineering literature related to monoliths,[15,21,22,39] the results of the lubrication analysis are rarely taken into account. An exception was Edvinsson,[40] who did note that a bubble with a flat rear and a hemispherical front must result in a pressure drop that is significant with respect to the viscous losses, although he did not consider the matter further.

Numerical Approach

The model problem studied in this work is a bubble moving in a round capillary of diameter d. The problem is considered to be two dimensional and axisymmetric. The gas-phase is not considered, that is, the gas-phase has negligible viscosity and density, compared to the liquid phase, and the gas-side velocity field is not solved. We have limited the Reynolds number to 900, and we assume that the liquid flow is laminar. The region considered is a single bubble between two regions of liquid moving at an average velocity U, equal to the sum of the gas and liquid superficial velocity. Van Baten and Krishna[17] used a periodic boundary condition on either end of a similar domain and found that the velocity profile quickly develops into a parabolic profile with a centerline velocity of twice the average velocity. Thus, the error made by explicitly imposing a parabolic profile is negligible, and on either end of the computational domain we have explicitly imposed a Hagen–Poiseuille profile. Assuming the same parabolic profile on both sides automatically ensures liquid volume conservation.

Governing equations

The equations of momentum conservation and continuity are given by

$$Re(u^* \cdot \nabla)u^* = -\nabla p^* + \nabla^2 u^* + BoCa^{-1}g^* \tag{3}$$

$$\nabla u^* = 0 \tag{4}$$

Equations 3 and 4 are already in their dimensionless form. Dimensionless quantities are denoted by an asterix. We scaled the equations on a viscous scale, $p^* = p(\mu U/d)^{-1}$, using the channel diameter d as the characteristic length.

The effect of gravity in Bretherton's problem is very limited. As demonstrated by Hazel and Heil[41] and Edvinsson and Irandoust,[34] the effect of gravity becomes noticeable only if the Bond number is significantly larger than unity. In this study, the effect of gravity was not taken into account.

The region is described in a reference frame in which the bubble is (almost) stagnant and in which the wall is moving at a constant velocity v^*. The bubble travels slightly faster than the surrounding liquid due to the wetting film between the bubble and the wall. This translational velocity of the bubble is part of the solution and cannot be specified beforehand.

The boundary conditions for the simulations are constant velocity at the wall

$$u_z^* = -v^*; \quad u_r^* = 0 \tag{5}$$

The parabolic Hagen–Poiseuille profile at the "inlet" and "outlet" becomes

$$u_z^* = 2 - 8r^{*2} - v^*; \quad u_r^* = 0 \tag{6}$$

Axial symmetry defines the velocity at the axis

$$\frac{\partial u_z^*}{\partial r^*} = 0; \quad u_r^* = 0 \tag{7}$$

Figure 2. Example mesh: top: initial mesh, bottom: converged mesh.

For incompressible flow, we may choose a reference pressure anywhere in the region, and conveniently we set the pressure in the gas bubble to zero. The pressure at the liquid side of the gas interface then depends on the interface curvature by

$$p^* = \frac{2}{Ca}\,\kappa^* \tag{8}$$

in which $\kappa^* = \kappa/d$ is the local Gaussian mean curvature of the interface. The angle of the interface with the axis was explicitly specified as $\pi/2$. Furthermore, at the gas–liquid interface the gradient of the tangential velocity with respect to the normal of the interface is given by

$$\frac{\partial u_t}{\partial n} = \nabla\gamma \tag{9}$$

In the absence of surface tension gradients, the righthand side of Eq. 9 is zero, and gives a no-shear boundary condition at the interface.

Finite-element formulation

The commercial finite element package FIDAP was used to solve the fluid dynamics problem described earlier. The region of interest was meshed with two types of elements. Far away from the interface, fixed elements were used, while close to the interface the grid nodes were free to move along lines called spines. Figure 2 shows an initial mesh and the mesh of a converged case, to illustrate the mesh movement. Only nine-point quadratic elements were used. After a steady state initialization using a rigid interface, the free-surface boundary conditions were specified, and the flexible grid nodes were allowed to move. The system of equations, which now included the position of the free surface nodes, was solved with the Newton–Raphson coupled solver, and a trapezoid implicit time integration was used until the bubble shape and the bubble velocity became constant. In the course of the simulation, the wall velocity v^* was periodically updated to keep the bubble in place.

The simulation was started from the same initial estimate for Reynolds numbers up to 200. For higher Reynolds numbers, the simulations did not converge because the standard Galerkin finite element methods became unstable. For the simulations of $Re > 200$, the converged solution for $Re = 200$, *ceteris paribus,* was used to start the transient simulation, in which a hybrid upwinding scheme was used that blends a first-order scheme with a higher-order scheme. For more details on the calculation of the blending factor, see the FIDAP manuals.[42]

Numerical Results

The majority of the calculations was performed using a grid with 3,395 nodes, and several representative calculations were performed with a grid of 6,255 nodes to check the grid-size dependence. As an example, Figure 3 shows the pressure at the wall for both grids for a representative case. No significant change in the pressure at the wall is observed upon doubling the amount of elements.

General characteristics of the axial pressure profile

For fully developed Hagen–Poiseuille flow of a single phase in a tube, the pressure drop is given by

$$\frac{\Delta p}{L} = \frac{16}{Re}\left(\frac{1}{2}\,\rho U^2\right)\frac{4}{d} \quad \text{or} \quad \frac{\partial p^*}{\partial z^*} = -32 \tag{10}$$

Far away from the bubble, the pressure drop per length is constant and has a value that is consistent with Hagen–Poiseuille flow. In the region of constant film thickness, the shear of the gas is negligible, and Figure 3 shows that the pressure at the wall is constant. The pressure drop over the entire bubble, however, is not zero, and the pressure difference over the frontal transition region is higher than the pressure drop over the rear transition region. The large oscillation at the rear of the bubble is caused by the presence of an inundation on the gas–liquid interface.

The total pressure drop over the entire computational domain can be decomposed into the frictional pressure drop of the liquid slug, and the pressure drop over the bubble

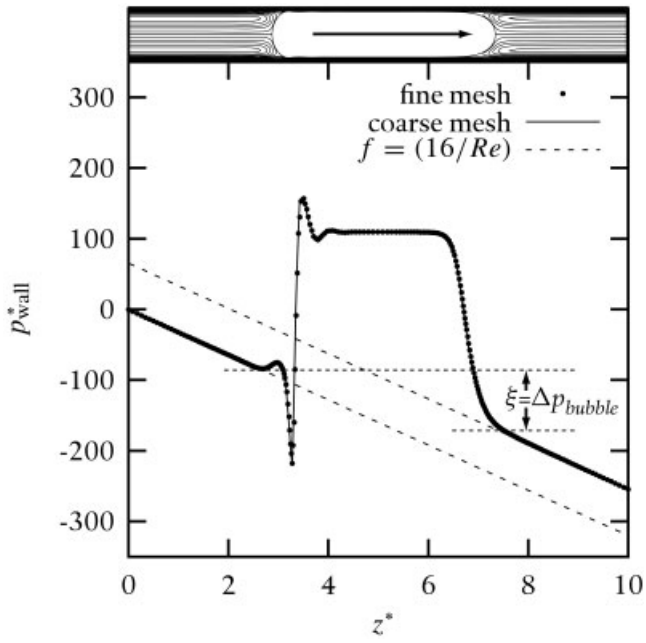

Figure 3. Wall pressure in the axial direction for Ca = 0.01, Re = 100, β_L = 0.65, L^* = 10.

The markers are computed values using a grid of 6255 nodes, and the line represents the computed values on a grid of 3395 elements. The dotted line has $(\partial p^*/\partial z^*) = -32$, which corresponds to developed laminar flow in a tube. On top, the bubble shape and the liquid streamlines for this case are shown, and the direction of flow is indicated.

$$\Delta p^* = -32L^*_{\text{slug}} + \Delta p^*_{\text{bubble}}(Re, Ca) \tag{11}$$

where $\Delta p^*_{\text{bubble}}$ describes the effects near the bubble, and is a function of Re and Ca. Note that in Eq. 11, the term $\Delta p^*_{\text{bubble}}$ now includes all the effects on the pressure drop over the bubble, including the effect of circulation in the slug and interfacial contributions. Because the frictional pressure drop is dominated by the slug region, we can model the effects of the bubble as part of the pressure drop in the slug to obtain

$$\Delta p^* = -32[1 + \xi(Re, Ca, L^*_{\text{slug}})]L^*_{\text{slug}} \tag{12}$$

The function ξ describes how the pressure drop is affected by the presence of bubbles. The parameter L^*_{slug} now appears in the functional form of ξ, because with increasing slug length, the relative contribution of ξ to the overall friction in the slug decreases. In fact, for infinitely long slugs, the effects of bubbles vanish

$$\lim_{L^*_{\text{slug}} \to \infty} \Delta p^* = -32L^*_{\text{slug}} \tag{13}$$

For a train of bubbles in a capillary, the dimensional pressure drop is then given by the pressure drop over the slugs alone

$$\frac{\Delta p}{L} = \beta_L f_{\text{slug}} \left(\frac{1}{2} \rho U^2 \right) \frac{4}{d} \tag{14}$$

where β_L, the dynamic holdup of liquid in the channel, is the fraction of channel length occupied by the slugs. Here, the slug friction factor is given by

$$f_{\text{slug}} = \frac{16}{Re}[1 + \xi(Re, Ca, L^*_{\text{slug}})] \tag{15}$$

In other words, an accurate model for pressure drop must include the bubble length—perhaps in the form of the bubble frequency—as a parameter. Experimentally, a wide range of slug lengths can be created in a given setup. The slug length is mainly determined by the hydrodynamics and geometry near the inlet of the channel, because once a volume of liquid is trapped between two bubbles, it cannot escape the slug it forms between the two sealing bubbles on either side. As a result, different slug lengths (or bubble frequencies) will be found in different setups, and this probably explains the spread in experimental data for capillary tubes in correlations based on homogeneous or two-phase multiplier (Lockhart–Martinelli) models.

The function ξ in Eq. 15 depends on Ca and Re. For low values of both of these dimensionless groups, that is, for $Ca \ll 1$ and $Ca \cdot Re = We \ll 1$, the Stokes-flow lubrication solutions may be used, and we rewrite Bretherton's result as

$$f_{\text{slug}} = \frac{16}{Re}\left[1 + \frac{7.16(3Ca)^{2/3}}{32L^*_{\text{slug}}Ca}\right] \tag{16}$$

In the remaining discussion of the numerical results, we will first validate the work with theory at low Re, and then continue with the simulations for higher Reynolds numbers to explore the effect of inertia on the pressure drop.

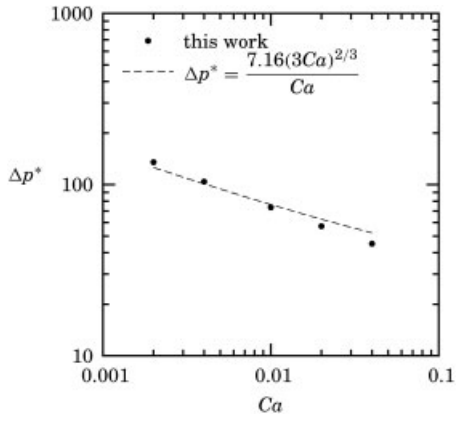

Figure 4. Pressure drop over the entire gas–liquid interface for simulations for $Re = 1$ (symbols).

The theoretical result of Bretherton is plotted as a dashed line.

Negligible inertia

The bubble pressure drop is plotted in Figure 4 for $Re = 1$, and the agreement with Eq. 2 is good. As the capillary number increases, the effect of interfacial forces decreases with respect to viscous forces. As a result, the contribution of the interfacial forces to the pressure drop relative to the pressure drop in the slug becomes smaller with increasing Ca.

Figure 4 shows that the pressure drop over the bubble ranges from 130 at $Ca = 0.002$ to 50 at $Ca = 0.04$. Comparison with the Hagen–Poiseuille pressure drop of 32 per channel diameter reveals that the excess pressure drop is roughly equivalent to the pressure drop of 2 to 4 channel diameters of developed flow. If the liquid slugs in Taylor flow are short, the presence of the bubbles has a measurable effect. For slugs that are five channel diameters long, the apparent friction factor is roughly fifty percent larger because of the bubbles. If the slugs are 50 channel diameters long, the apparent friction factor is increased only by five percent, and the bubble pressure drop can probably be ignored.

Effect of inertia

Figure 5 shows the effect of inertia on the film thickness. The decrease in film thickness up to Reynolds numbers of about 100, followed by an increase for higher Reynolds numbers is in agreement with the numerical results of Giavedoni and Saita[35,36] for low Re, the numerical results of Heil[37] for the similar 2-D planar case for Re up to 280, and the experimentally observed film thickening at high Re by Aussilous and Quére.[38] Increasing the Reynolds number also changes the shape of the bubbles. Especially at higher Capillary numbers the interfacial forces are not large enough to maintain the hemispherical shape of the caps. With increasing Re, the nose of the bubble is elongated and the rear of the bubble is flattened, see Figure 6.

Heil reported an increase in pressure drop in the transition region of the front of the bubble with increasing Re. In Figure 7, the impact of inertia on the pressure drop over the bubble

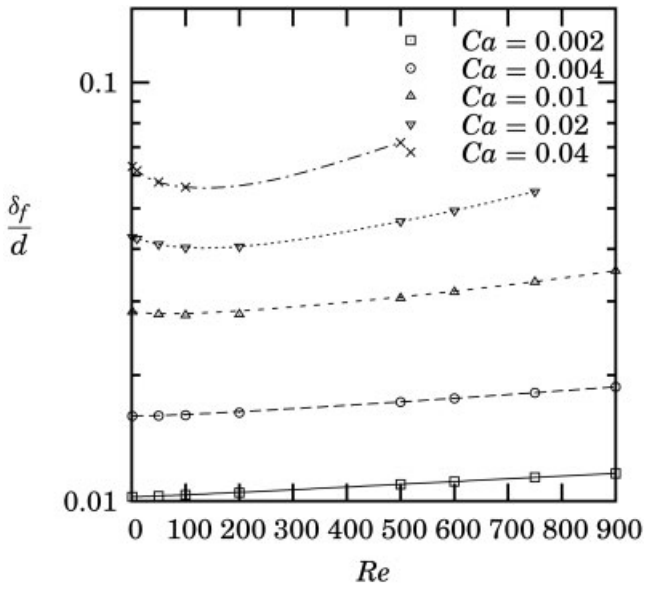

Figure 5. Film thickness at the middle of the bubble vs. the Reynolds number for simulations at different *Ca*.

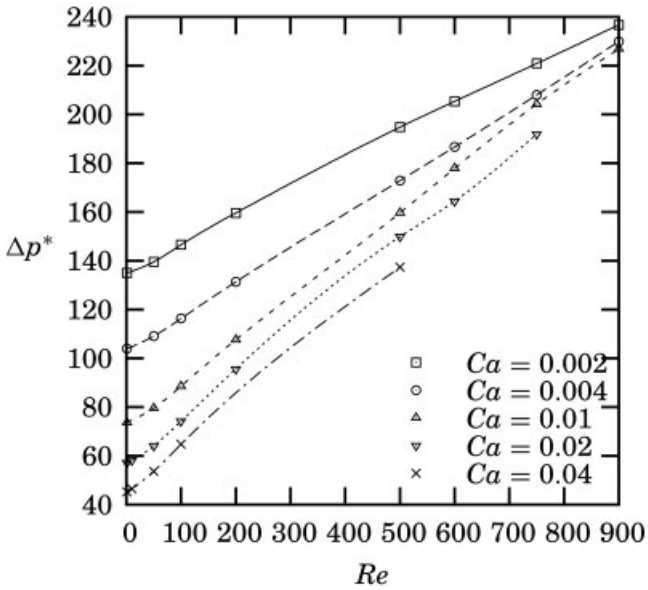

Figure 7. Pressure drop over the bubble vs. Reynolds number for simulations at different *Ca*.

alone is plotted. Clearly, the pressure drop increases with increasing Reynolds number. The effect is slightly stronger for high Capillary numbers.

In Figure 8, the pressure drop over the entire region, including the slugs, is plotted versus the Reynolds number. If we ignore the effect of the bubble and flow development on the flow in the slug ($\xi = 0$), the dimensionless pressure drop in the slug is given by the Hagen–Poiseuille value $\Delta p^* = 32L^*_{\text{slug}}$, where L^*_{slug} is the dimensionless length of the liquid slug. In Figure 8, the deviation from this simple approximation is plotted. The same trend as for the bubble pressure drop is observed: (1) increasing the Capillary number decreases the pressure drop, (2) increasing the Reynolds number increases the pressure drop, and (3) with increasing *Ca*, the effect of inertia increases.

Comparison of Figures 7 and 8 reveals that the effect of inertia for the entire domain is smaller than for the bubble alone. At $Ca = 0.002$, the bubble pressure drop increases by 100 from $Re = 0$ to $Re = 900$, while the pressure drop over the entire domain only increases by 40. At low Reynolds numbers, the values are marginally different, while for high Reynolds numbers, the dramatic increase in pressure drop at the interface is not observed for the entire region.

Inertial effects are most important in the circulation region.

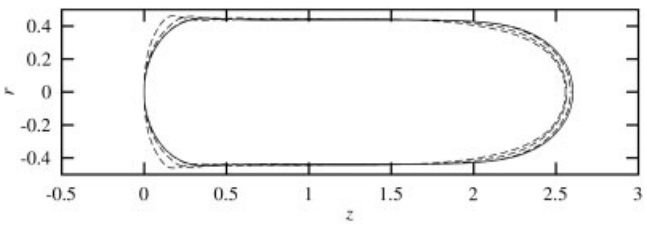

Figure 6. Shape of the gas–liquid interface for *Re* = 1, 10, 100, 200 at *Ca* = 0.04.

Figure 9 shows the pressure distribution and streamlines at the rear of the bubble. At low Reynolds number, the interfacial pressure increases monotonically from the flat film to the tip of the bubble. Furthermore, all the lines of constant pressure that originate at the bubble interface extend to the channel wall, which indicates that the entire interfacial pressure adds to the overall pressure drop. For higher *Re*, the inertia of the circulating liquid gives rise to a large dynamic pressure buildup that changes in the bubble shape in accordance with the Laplace pressure term of Eq. 8. In fact, on the flattened hemisphere at

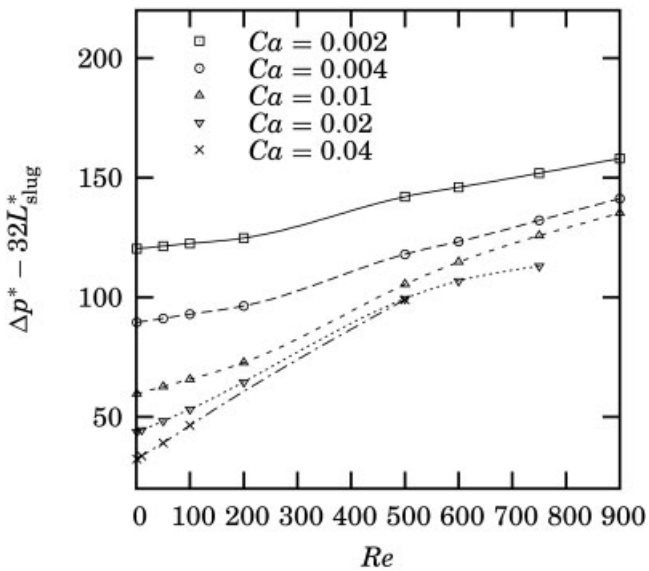

Figure 8. Pressure drop from the inlet to the outlet of the computational domain vs. Reynolds number for several *Ca*.

The contribution of fully developed flow in the slug has been subtracted, where the length of the slug is defined as the region without any gas in the cross section.

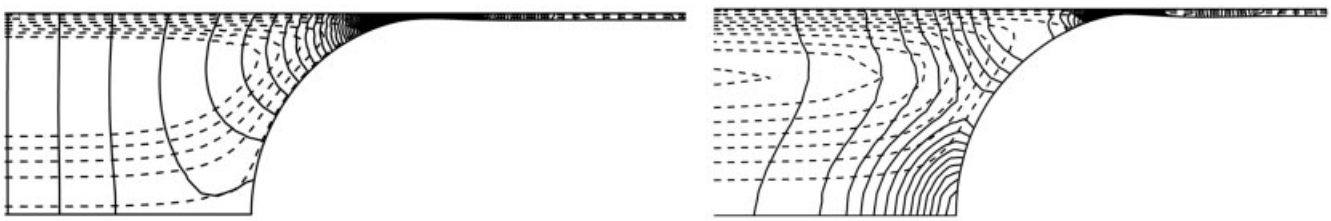

Figure 9. Contours of pressure (solid lines) and stream function (dashed lines) for $Ca = 0.004$.

the rear of the bubble a minimum in the interfacial pressure is observed. Near this minimum, the streamlines of the circulating liquid are less curved, and, hence, a lower inertial or centrifugal pressure affects the bubble shape. Only the pressure difference from the film to this minimum extends into the slug. The isobars of high pressure close to the tip of the bubble do not extend to the channel wall, and as a result do not contribute to the overall pressure drop. The minimum can also been seen in the simulations of Heil[37] for 2-D planar flow at the front of a 2-D bubble. In this work, the effect was found to be much more pronounced near the rear of the bubbles, which is consistent with the fact that at the rear, the bubble shape is more deformed by inertial effects. Figure 9 clearly shows that the pressure effect of inertia near the axis is local, and this explains the lower effect of inertia on the pressure drop over the entire domain.

Experimental

The vertical two-phase up-flow pressure drop was measured in a capillary of 2.3 mm internal diameter. The setup is depicted in Figure 10a. A special inlet device, of which a cross section is drawn in Figure 10b, was used for feeding the gas and liquid into the capillary.

The liquid entered the system through two inlets at the bottom of the device. The internal diameter of the device was 35 mm at the bottom and slowly decreased over a length of 100 mm to the diameter of the capillary channel. The gas was injected through a flat tip hypodermic needle into the liquid approximately 50 mm below the inlet of capillary. By using different sized needles—three different ones were used in this study—the size of the bubbles leaving the needle could be adjusted. As the superficial velocity of the liquid is still very low at the tip of the needle, the impact of the liquid velocity on the size of the bubble was found to be moderate.

The liquid was continuously pumped through the channel by two ISCO 500D syringe pumps at 0–200 mL/min. A system of check valves allowed one pump to be refilled while the other was delivering liquid to the channel. The gas was delivered at 0–200 mL/min by two digital Brooks 5850S® mass flow controllers. From the inlet upwards, the channel consisted of a pressure tap segment, a segment of straight channel and a second pressure tap. Each segment had a tapered end on top that was polished such that it fitted seamlessly into the widening bottom of the next segment, so a perfectly aligned, seamless channel was formed. In the pressure tap elements, a slit of less than 0.5 mm connected the capillary to a larger chamber in which the pressure was measured via liquid filled lines using a Druck LPX 7000-XYZ differential pressure sensor, see Figure 10c.

In the middle of the capillary channel, two infrared sensors were mounted that allowed the discrimination of passing bubbles from passing slugs by the difference in IR absorption between gas and liquid.[43] The infrared sensors have the benefit over conductivity methods of being able to efficiently detect liquids other than water. The signal from the IR sensors was processed with a binary gate (1 = bubble, 0 = slug). The bubble and slug velocity were calculated from the cross-correlation of these binary signals, and finally using the calculated velocity the length of each passing bubble and slug was calculated.

The proper operation of the system was verified by doing liquid-only pressure drop measurements. The friction factor obtained from these experiments was within 5% of the Hagen–Poiseuille value of $16/Re$. It is well known that up-flow Taylor flow is unstable.[21] As a result, the compressible volume before the needle must be minimized. However, during startup of the system, liquid leaked through the needle causing an irregular gas flow into the needle. This dramatically broadened the spread in slug lengths, and could be resolved only by mounting a small liquid catcher just below the inlet system. Installing this liquid catcher introduced a compressible gas volume, and as a result the time required to achieve steady state flow was increased: it took up to 3 min before the pressure drop, bubble length and slug length were stable.

Once steady state was achieved, the bubble and slug lengths were measured for 30–60 s, and subsequently 100–200 recordings of pressure drop, temperature (inlet and outlet), gas velocity and liquid velocity were made. Experiments were performed using three different liquids: water, decane and tetradecane. The relevant physical properties of the liquids at 293 K are given in Table 1. *Ceteris paribus,* the Capillary number in air/water, air/decane and air/tetradecane relate to each other as roughly 1:3:7, whereas the Reynolds numbers relate roughly as 1:0.8:0.3.

Results

Bubble and slug lengths

Using the inlet section described above, it was possible to vary the bubble and slug lengths over a wide range, see Figure 11, where an overview of the experimental range is given. The smallest and largest needle created bubbles of approx. 5 and 15 mm in length inside the channel, respectively, leading to aspect ratios L^*_{bubble} of 2 to 7. If the liquid velocity was too low or too high, the bubbles started to coalesce before entering the chan-

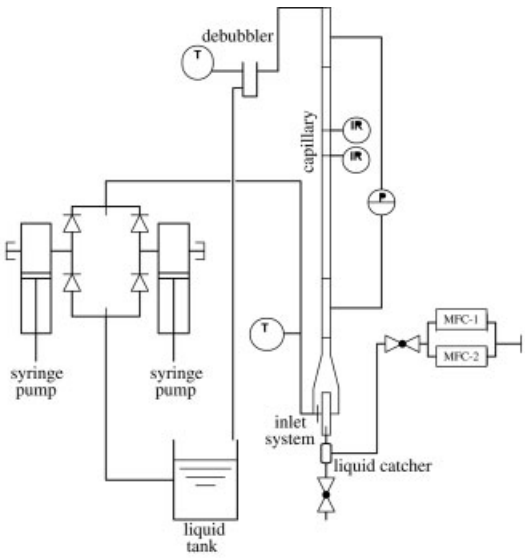

(a) overview

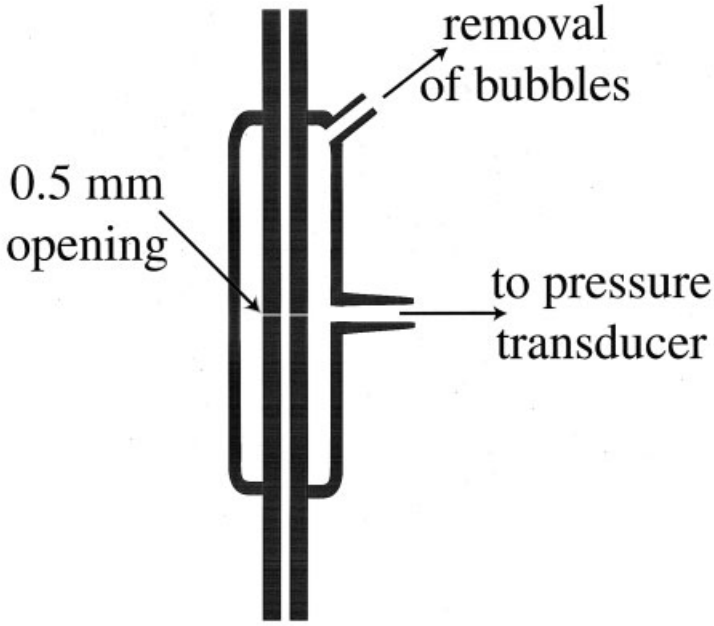

(c)

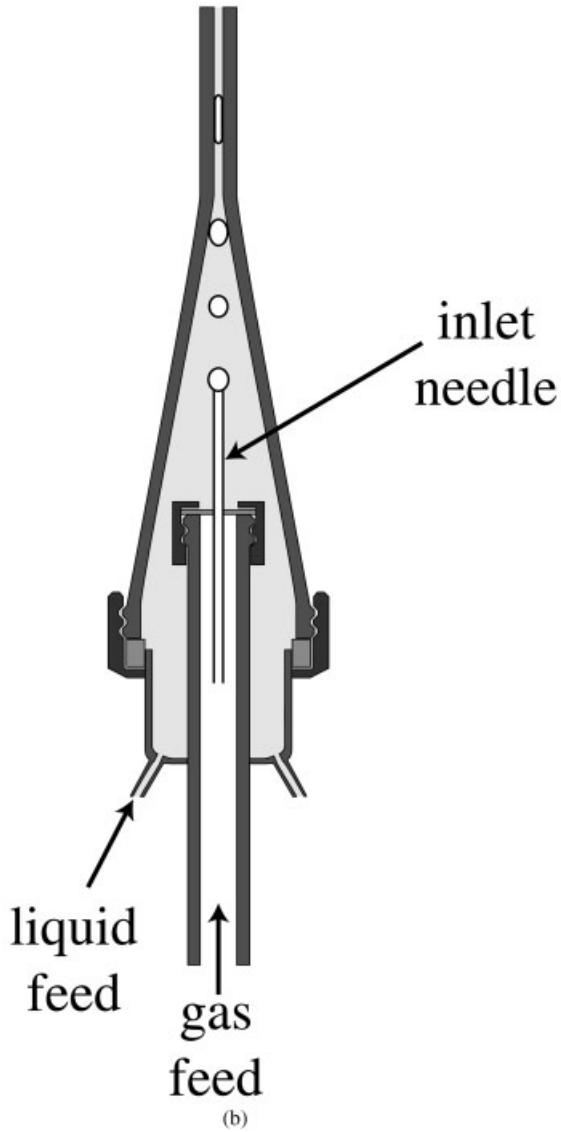

(b)

Figure 10. Experimental setup.

Table 1. Physical Properties for the Liquids used at 293 K

Liquid	ρ_L (kg/m^3)	μ_L (MPa · s)	γ (N/m)
Water	996	1.01	0.073
Decane	730	0.924	0.024
Tetradecane	762	2.32	0.026

nel. Roughly, stable slug and bubble sizes were found when $0.25 < u_{Ls}/u_{Gs} < 2$.

Bubble velocity

The measured bubble velocity u_B is plotted against the sum of gas and liquid superficial velocity U, in Figure 12. The excess velocity of the bubbles, $u_B - U$, may be calculated from the thickness of the stagnant film surrounding the bubble, which in turn is a monotonically increasing function of the Capillary number. Figure 12 shows that the excess velocity indeed increased with velocity. At a given velocity U the excess velocity was lowest for water (high γ, so low Ca), and highest for tetradecane (high μ, so high Ca). So, the right trend with respect to flow rate and fluid properties was found, but the scatter in the excess velocity was large. (Note that we substract two very similar experimental values u_B and U)

Pressure drop

In Figure 13, the friction factor, calculated from experiments by

$$f_{obs} = \frac{\left(\frac{\Delta p}{L}\right)_{(tot)} - \beta_L \rho g L}{\left(\frac{1}{2}\rho_L U^2\right)\left(\frac{4}{d}\right)\beta_L} \tag{17}$$

multiplied with the Reynolds number is plotted vs. the dimensionless slug length $L^*_{slug} = L_{slug}/d$. The experimental data clearly show that for each liquid, the friction factor is a function of slug length. Moreover, the results suggest that the slug length alone is sufficient to describe the experimental results for a given liquid, and no effect of the velocity is observed. This is surprising, because the numerical results suggest that Re and Ca have a strong impact on the slug friction factor, and both Ca and Re are linear functions of velocity. The experiments were conducted for a wide range of velocities, so the data for a given liquid were obtained for a wide range of both Ca and Re.

On the other hand, the observed dependence of pressure drop on the slug length is different for the different fluids. For water, which has the highest surface tension, the pressure drop is affected the most, while the data for the organic liquids show a less pronounced effect. Moreover, tetradecane, which is more

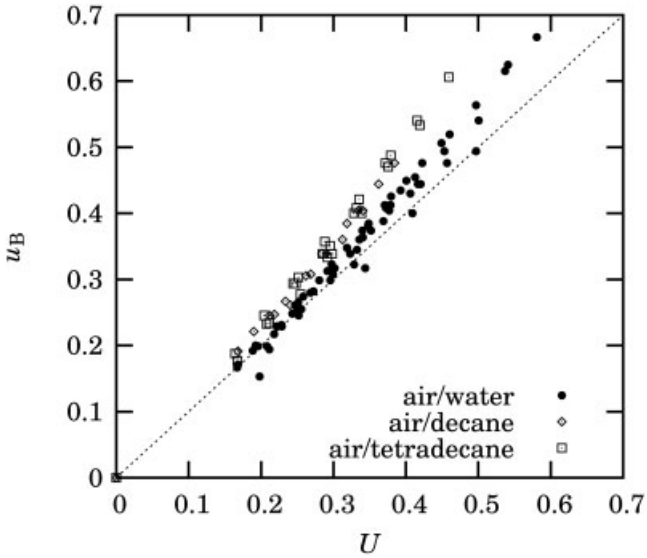

Figure 12. Bubble velocity u_B, measured using the infrared sensors, to the sum of gas and liquid superficial velocities, U.

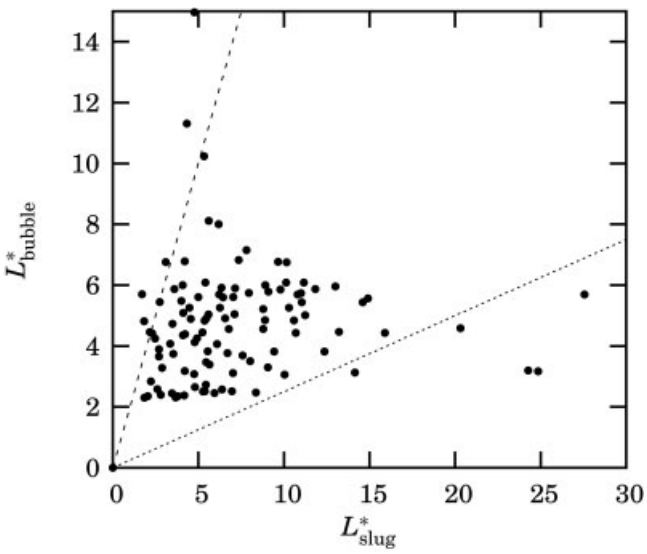

Figure 11. Experimental slug aspect ratio L^*_{slug} vs. bubble aspect ratio L^*_{bubble}.

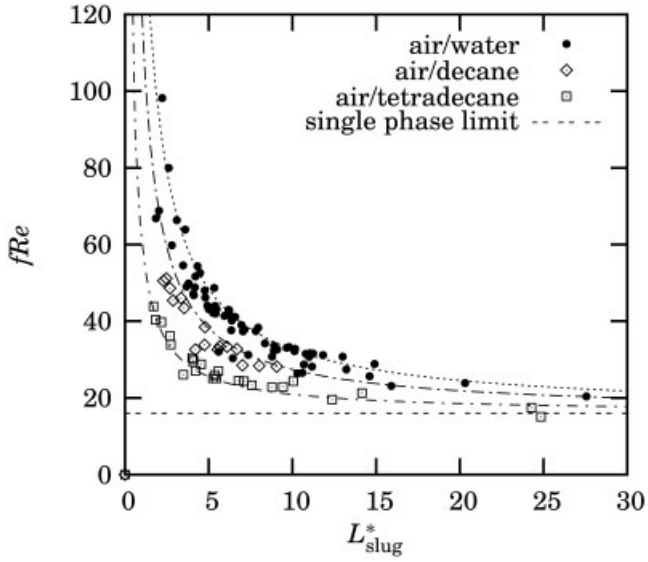

Figure 13. (f Re) as a function of dimensionless slug length. Channel dia. d = 2.3 mm.

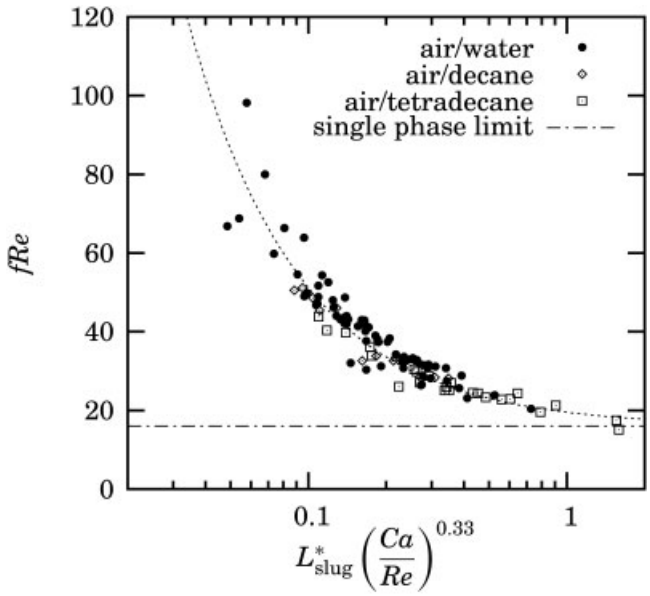

Figure 14. Final pressure drop correlation, ($f\,Re$) as a function of the dimensionless group $L^*_{slug}(Ca/Re)^{0.33}$: channel dia. $d = 2.3$ mm.

viscous than decane, shows the smallest increase from the single phase limit $f = 16/Re$.

The fact that the friction factor is independent of velocity, but does vary with liquid properties can be modeled by using the ratio of the capillary number and the Reynolds number as a parameter. This dimensionless group, $Ca/Re = \mu^2/\rho d\gamma$, is independent of velocity. In other words, the excess pressure caused by the bubble ξ is likely to have the following functional form

$$\xi = a\left(\frac{1}{L^*_{slug}}\left(\frac{Re}{Ca}\right)^b\right) \tag{18}$$

The parameters a and b were determined by nonlinear regression, and an expression was found that satisfactorily described all the data, see Figure 14.

$$f = \frac{16}{Re}\left[1 + 0.17\,\frac{1}{L^*_{slug}}\left(\frac{Re}{Ca}\right)^{0.33}\right] \tag{19}$$

Bretherton's equation for the pressure drop at low Re, Eq. 16, showed that the additional term in the friction factor is inversely proportional to $L^*_{slug}Ca^{1/3}$, and our experimental results agree.

Discussion

The numerical analysis of Taylor flow revealed that for short slugs, the Laplace pressures are significant with respect to the viscous losses in the slug. The experiments confirmed the importance of accounting for the contribution of the Laplace pressures in the slug-length-averaged friction factor. The experimentally observed increase in pressure drop, however, is larger than found in the finite-element calculations. In Figure 15, the same dimensionless plot as used for the experimental data is made for the numerical data. Apparently, the numerical data can be correlated using the same dimensionless group (under the condition that $Re > 50$), which supports the experimental finding that the excess friction in the slug can be described by the parameter Ca/Re. A correlation that agrees with the numerical data can be constructed by replacing the constant 0.17 in Eq. 19 by 0.07, so there is a systematic difference of a factor of 2.5.

This large difference cannot be attributed to experimental error. The likely cause of the differences is a Marangoni effect. The finite-element calculations were performed assuming clean liquids. In the experimental setup, no attempt was made to work in ultra-pure conditions, and impurities were likely to be present. Possible sources for impurities are (1) the bulk liquids themselves, (2) lubricants in the gas feed, and (3) dissolved weakeners from the tubing. Moreover, after switching from organic liquids to water and vice versa, traces of liquid are likely to be left behind in the syringe pumps, even after rinsing several times.

If the no-shear boundary condition at the gas–liquid interface in the transition zone is replaced by a no-slip boundary condition, Ratulowski and Chang[28] showed that the Bretherton solution can be used with the transformation $Ca \rightarrow (1/4)Ca$. The pressure drop over the bubble in the lubrication analysis of Bretherton, Eq. 2, then transforms as $\Delta p \rightarrow 4^{2/3}\Delta p$. The factor $4^{2/3}$ is practically equal to the factor 2.5, which describes the difference between the experimental and numerical data. The analysis by Ratulowski and Chang did not include inertia. The numerical results (see Figure 9) showed that the contributions to the overall pressure losses are dominated by the fluid mechanics in the transition zone for which their transformation

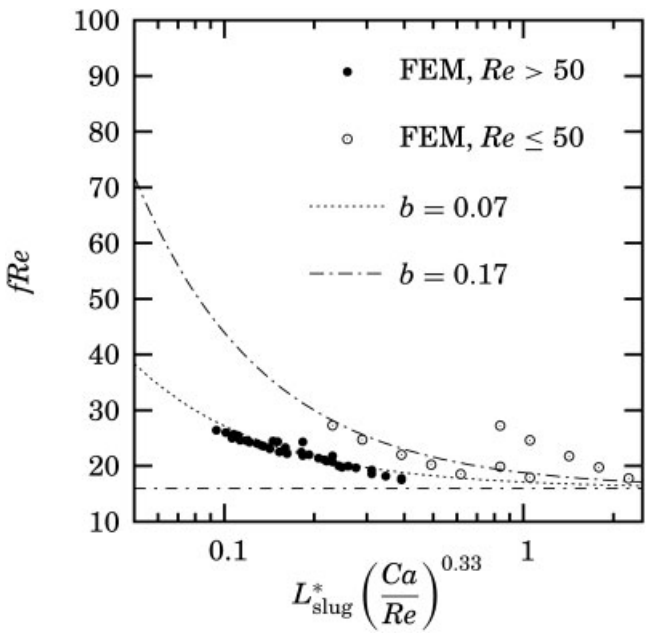

Figure 15. Numerical frictional pressure drop plotted using the same dimensionless groups as used for the experimental data.

$100 < Re < 900$, $0.002 < Ca < 0.04$, $8 < L/d < 12$. The lines are based on Eq. 19 with $b = 0.17$ and on 19 with $b = 0.07$ to reflect the absence of impurities in the simulations.

was derived. In this zone the assumption of strong Marangoni effects is not unreasonable, because the concentration gradients of the surfactants are most likely highest near the stagnation points on the interface, that is, in the transition zone. The concentration gradients close to the bubble tip are irrelevant for the overall pressure drop (see Figure 9). In the film, the surfactant concentrations are most likely uniform, and the experimental finding that the bubble length may be ignored supports that we assume no-shear in the film between the bubble caps. (Stebe and Barthes-Biesel[30] actually found another regime, in aqueous systems with highly elevated concentrations of the surfactant sodium dodecyl benzene sulphonate, where the pressure drop was actually found to increase with increasing bubble length.) Clearly, the last word has not yet been said about the combined effect of Marangoni stresses and inertia in Bretherton's problem.

The numerical results indicate that the excess pressure drop depends on liquid properties through Ca/Re, which is independent of velocity, and the experimental results confirm this. Finally, it should be noted that the empirical correlation Eq. 19 is valid only at high Re, or more specifically for $Ca = \mathbb{O}(0.01)$ and $Re = \mathbb{O}(100)$ which may also be written as $We = \mathbb{O}(1)$. When Re is close to unity, the original equation of Bretherton, Eq. 2 or 16, is more appropriate.

Implications for multiphase monoliths

With the present pressure-drop model, pressure-drop measurements can be used to obtain an estimate of the slug lengths found in monolith reactors.

Heiszwolf et al.[44] measured the length of bubbles and slugs inside a monolith using conductivity. Mantle et al.[45] used MRI to measure velocity and length of bubbles and slugs inside a monolith. Both experimental setups were very different in their feed hydrodynamics, but the order of magnitude for the slug length was similar, that is, 2–6 times the channel diameter. For such short slugs, the interfacial phenomena are significant. The correlation developed in this work can be used to get an estimate of the slug lengths from experimental pressure drop data if the slugs are shorter than 10 times the channel diameter.

Previous attempts to model pressure drop experiments in monoliths have used segmented flow models that consider the static head and the friction factor $16/Re$ in the slugs. Such models under-predicted the experimental pressure drop, and the deviations between model and experiment were attributed to contraction/expansion losses,[22,39] or to a gas–liquid interaction[21] that did not depend on surface tension, or to secondary flow development inside the slugs.[15] Heiszwolf et al.[15] used $f = C/Re$ for both the bubbles and the slugs with reasonable success and noted that "Apparently, the loss of friction by introducing gas bubbles is counteracted by the increased friction of the liquid slug." Irandoust et al.[46] have, on the other hand, found that $16/Re$ for the slugs alone gave accurate results. The understanding developed in this work suggests that Irandoust et al. performed experiments under such conditions that long slugs were present.

Conclusions

In this article, the pressure drop of a train of bubbles in a capillary channels has been investigated. By using a finite-element description of a single bubble between liquid slugs, the problem was investigated numerically. The results for low Reynolds numbers agreed well with the classical lubrication analysis. Increasing the Reynolds number allowed for the investigation of the behavior of low viscosity liquids at high velocities. A significant increase in pressure drop was found as inertia becomes more important. Experimentally, the pressure drop was studied in a capillary using different liquids in a setup that allowed the independent variation of bubble and slug length.

An important observation is that apart from viscous, inertial and interfacial forces, the geometry of the bubble train flow has to be taken into account. More precisely, the aspect ratio of the slugs that separate the bubbles has a profound impact on the friction factor. This can be interpreted physically by realizing that in the middle of the slug, the flow profile across the channel resembles Hagen–Poiseuille flow, while at the ends of the slug, the flow pattern is significantly altered by the presence of the bubbles. Furthermore, for each slug a Laplace pressure term must be included to account for the pressure drop caused by the bubble.

The influence of the slug length can easily be transformed into a dependence on the bubble frequency. Thus, more bubbles per unit channel length will result in a higher pressure drop. The theoretical foundations of the importance of the slug length—including quantitative estimates—were already laid out forty years ago. Most of the experimental data in the open literature, however, are still reported without bubble frequencies and the current engineering models do not take these effects into account. As a result, these engineering models fail to predict the pressure drop accurately in capillaries.

Although the numerical and experimental data show the same trends, the experimental data deviates systematically from the simulations. This deviation can be explained by Marangoni effects, that are not taken into account in the simulations, but are likely to be present in the experiments.

The slug length is an important parameter in the design of monolith reactors, and it need to be determined experimentally. The pressure drop modeling presented in this work allows the (average) slug length to be obtained from pressure drop experiments, which is a much easier method than tomography or conductivity.

Acknowledgment

This work was financially supported by grant DST 66.4653 of the Dutch Foundation for Technological Science (STW-NWO).

Notation

d = diameter m
f = friction factor
g = gravitational constant, m/s^2
L = length, m
n = normal to the gas–liquid interface
p = pressure, Pa
r = radius, m
u = velocity, m/s
U = sum of gas and liquid superficial velocity, m/s

Greek letters

β = dynamic holdup
γ = surface tension, N/m

δ = film thickness, m
ε = holdup
κ = curvature
λ = length transition region, m
μ = viscosity, Pa s
ν = wall velocity
ρ = density, kg/m^3
ξ = excess pressure term

Dimensionless groups

Bo = Bond number ($=\rho g d^2/\gamma$)
Ca = Capillary number ($=\mu U/\gamma$)
Fr = Froude number ($=U^2/gd$)
Re = Reynolds number ($=\rho U d/\mu$)
We = Weber number ($=\rho U^2 d/\gamma$)

Subscripts

B = bubble
c = channel
Ca = capillary-scale
G = gas
L = liquid
s = superficial
S = slug
t = tangential
TP = two-phase

Literature Cited

1. Moulijn JA, Cybulski A. (eds.) *Structured catalysts and reactors.* Marcel Dekker; 1998.
2. Boger T, Roy S, Heibel AK, Borchers O. A monolith loop reactor as an attractive alternative to slurry reactors. *Catalysis Today.* 2003;79–80:441–451.
3. Duduković MP, Larachi F, Mills PL. Multiphase catalytic reactors: A perspective on current knowledge and future trends. *Catalysis Reviews—Sci and Eng.* 2002;44:123–246.
4. de Deugd RM, Chougule RB, Kreutzer MT, Meeuse FM, Grievink J, Kapteijn F, Moulijn JA. Is a monolithic loop reactor a viable option for Fischer-Tropsch synthesis? *Chem Eng Sci.* 2003;58:583–591.
5. Khassin AA, Yurieva TM, Sipatrov AG, Kirillov VA. Chermashentseva GK, Parmon VN, Fischer-Tropsch synthesis using a porous catalyst packing: experimental evidence of an efficient use of permeable composite monoliths as a novel type of the Fischer-Tropsch synthesis catalyst. *Catalysis Today.* 2003;79–80:465–470.
6. Mazzarino I, Baldi G. Liquid phase hydrogenation on a monolith catalyst. In: Kulkarni B, Mashelkar R, Sharma M. eds. *Recent Trends in Chemical Reaction Engineering,* New Dehli: Wiley Eastern Ltd.; 1987;181–189.
7. Kreutzer MT, Du P, Heiszwolf JJ, Kapteijn F, Moulijn JA. Mass transfer characteristics of three phase monolith reactors. *Chem Eng Sci.* 2001;56:6015–6023.
8. Nijhuis TA, Kreutzer MT, Romijn ACJ, Kapteijn F, Moulijn JA. Monolith catalysts as efficient three-phase reactors. *Chem Eng Sci.* 2001;56:823–829.
9. Vergunst T, Kapteijn F, Moulijn J. Optimization of geometric properties of a monolithic catalyst for the selective hydrogenation of phenylacetylen. *Ind. and Eng Chem Res.* 2001;40:2801–2809.
10. Boger T, Zieverink MM, Kreutzer MT, Kapteijn F, Moulijn JA, Addiego WP. Monolithic catalysts as an alternative to slurry systems: Hydrogenation of edible oil. *Ind and Eng Chem Res.* 2004;43:2337–2344.
11. Broekhuis RR, Budhlall BM, Nordquist AF. Monolith catalytic process for producing sorbitol: Catalyst development and evaluation. *Ind and Eng Chem Res.* 2004;43:5146–5155.
12. Machado RM, Parrillo DJ, Boehme RP, Broekhuis RR. Use of a monolith catalyst for the hydrogenation of dinitrotoluene to toluenediamine. *U. S. Patent.* 1999;US 6005143.
13. Bretherton FP. The motion of long bubbles in tubes. *J of Fluid Mechanics.* 1961;10:166–168.
14. Taylor GI. Deposition of a viscous fluid on the wall of a tube. *J of Fluid Mechanics.* 1961;10:161–165.
15. Heiszwolf JJ, Engelvaart LB, van der Eijnden MG, Kreutzer MT, Kapteijn F, Moulijn JA. Hydrodynamic aspects of the monolith loop reactor. *Chem Eng Sci.* 2001;56:805–812.
16. Berčič G, Pintar A. The role of gas bubbles and liquid slug lengths on mass transport in the Taylor flow through capillaries. *Chem Eng Sci.* 1997;52:3709–3719.
17. Van Baten JM, Krishna R. CFD simulations of mass transfer from Taylor bubbles rising in circular capillaries. *Chem Eng Sci.* 2004;59:2535–2545.
18. Kreutzer MT, Heiszwolf JJ, Kapteijn F, Moulijn JA. Pressure drop of taylor flow in capillaries: impact of slug length. In: Proceedings of the 1st International Conf on microchannels and minichannels, Rochester NY, USA.: ASME. 2003;153–159.
19. Khan SA, Günther A, Schmidt MA, Jensen KF. Microfluidic synthesis of colloidal silica. *Langmuir.* 2004;20:8604–8611.
20. Günther A, Khan SA, Thalmann M, Trachsel F, Jensen KF. Transport and reaction in microscale segmented gas liquid flow. *Lab on a Chip.* 2004;4:278–286.
21. Reinecke N, Mewes D. Oscillatory transient two-phase flows in single channels with reference to monolithic catalyst supports. *Intl J of Multiphase Flow.* 1999;25:1373–1393.
22. Grolman E, Edvinsson R, Stankiewicz A, Moulijn J. Hydrodynamic instabilities in gas-liquid monolithic reactors. In: Proceedings of the ASME Heat Transfer Division, ASME. 1996;334-3:171–178.
23. Kreutzer MT, Bakker JJW, Kapteijn F, Moulijn JA, Verheijen PJT. Scaling-up multiphase monolith reactors: Linking residence time distribution and feed maldistribution using isobars. *Ind and Eng Chem Res.* 2005; accepted for publication (DOI:10.1021/ie0492350).
24. Horvath C, Solomon BA, Engasser HM. Measurement of radial transport in slug flow using enzyme tubes. *Ind and Eng Chem Fundamentals.* 1973;121:431–439.
25. Lockhart RW, Martinelli RG. Proposed correlations for isothermal two-phase two-component flow in pipes. *Chem Eng Prog.* 1949;45:39–48.
26. Chen IY, Yang KS, Wang CC. An empirical correlation for two-phase frictional performance in small diameter tubes. *Intl J of Heat and Mass Transfer.* 2002;45:3667–3671, [DOI].
27. Chang HC. Bubble/drop transport in microchannels. In: *the MEMS Handbook,* Boca Raton: CRC Press. 2002;chapter 11.
28. Ratulowski J, Chang HC. Marangoni effects of trace impurities on the motion of long gas bubbles in capillaries. *J of Fluid Mechanics.* 1990;210:303–328.
29. Park CW. Influence of soluble surfactants on the motion of a finite bubble in a capillary tube. *Physics of Fluids.* 1992;A 4:2335–2346.
30. Stebe KJ, Barthes-Biesel D. Marangoni effects of adsorption-desorption controlled surfactants on the leading end of an infinitely long bubble in a capillary. *J of Fluid Mechanics.* 1995;286:25–48.
31. Shen EI, Udell KS. A finite element study of low Reynolds number two-phase flow in cylindrical tubes. *J of Appl Mech.* 1985;52:253–256.
32. Reinelt DA. The rate at which a long bubble rises in a vertical tube. *J of Fluid Mechanics.* 1987;175:557–565.
33. Ratulowski J, Chang HC. Transport of bubbles in capillaries. *Physics of Fluids A.* 1989;1:1642–1655.
34. Edvinsson RK, Irandoust S. Finite-element analysis of Taylor flow. *AIChE J.* 1996;42:1815–1823.
35. Giavedoni MD, Saita FA. The axisymmetric and plane case of a gas phase steadily displacing a Newtonian liquid—A simultaneous solution to the governing equations. *Physics of Fluids.* 1997;9:2420–2428.
36. Giavedoni MD, Saita FA. The rear meniscus of a long bubble steadily displacing a Newtonian liquid in a capillary tube. *Physics of Fluids.* 1999;11:786–794.
37. Heil M. Finite Reynolds number effects in the Bretherton problem. *Physics of Fluids.* 2001;13:2517–2521.
38. Aussilous P, Quére D. Quick deposition of a fluid on the wall of a tube. *Physics of Fluids.* 2000;12:2367–2371.
39. Satterfield CN, Özel F. Some characteristics of two-phase flow in a monolithic catalyst structures. *Ind and Eng Chemistry Fund.* 1977;16:61–67.
40. Edvinsson R. Monolith Reactors in Three-Phase Processes. Chalmers University of Technology, Goteborg; Sweden; 1994. Ph. D. Thesis.
41. Hazel AL, Heil M. The steady propagation of a semi-infinite bubble

into a tube of elliptical or rectangular cross-section. *J of Fluid Mechanics.* 2002;470:91–114.
42. FIDAP manuals, *FIDAP 8 Theory manual.* Fluent, Inc., Lebanon, USA; 1998.
43. Wolffenbuttel BMA, Nijhuis TA, Stankiewicz A, Moulijn JA. Novel method for non-intrusive measurement of velocity and slug length in two- and three-phase slug flow in capillaries. *Measurement Sci and Technol.* 2002;13:1540–1544.
44. Heiszwolf JJ, Kreutzer MT, van der Eijnden MG, Kapteijn F, Moulijn JA. Gas-liquid mass transfer of aqueous Taylor flow in monoliths. *Catalysis Today.* 2001;69:51–55.
45. Mantle MD, Sederman AJ, Gladden LF. Dynamic MRI visualization of two-phase flow in a ceramic monolith. *AIChE J.* 2002;48:909–912.
46. Irandoust S, Andersson B, Bengtsson E, Silverstrom M. Scale up of a monolytic catalyst reactor with two-phase flow. *Ind and Eng Chemistry Res.* 1989;28:1489–1493.

Manuscript received Oct. 11, 2004, and revision received Dec. 22, 2004.